Research Letter **DOI:** 10.15541/jim20240165

Single- and Two-band Transport Properties Crossover in Bi_2Te_3 Based Thermoelectrics

MENG Yuting, WANG Xuemei, ZHANG Shuxian, CHEN Zhiwei, PEI Yanzhong

(Interdisciplinary Materials Research Center, School of Materials Science and Engineering, Tongji University, Shanghai 201804, China)

Abstract: Based on Peltier effect, Bi_2Te_3-based alloy is widely used in commercial solid-state refrigeration at room temperature. The mainstream strategies for enhancing room-temperature thermoelectric performance in Bi_2Te_3 focus on band and microstructure engineering. However, a clear understanding of the modulation of band structure and scattering through such engineering remains still challenging, because the minority carriers compensate partially the overall transport properties for the narrow-gap Bi_2Te_3 at room temperature (known as the bipolar effect). The purpose of this work is to model the transport properties near and far away from the bipolar effect region for Bi_2Te_3-based thermoelectric material by a two-band model taking contributions of both majority and minority carriers into account. This is endowed by shifting the Fermi level from the conduction band to the valence band during the modeling. A large amount of data of Bi_2Te_3-based materials is collected from various studies for the comparison between experimental and predicted properties. The fundamental parameters, such as the density of states effective masses and deformation potential coefficients, of Bi_2Te_3-based materials are quantified. The analysis can help find out the impact factors (*e.g.* the mobility ratio between conduction and valence bands) for the improvement of thermoelectric properties for Bi_2Te_3-based alloys. This work provides a convenient tool for analyzing and predicting the transport performance even in the presence of bipolar effect, which can facilitate the development of the narrow-gap thermoelectric semiconductors.

Key words: thermoelectric material; Bi_2Te_3-based alloy; two-band model; narrow-gap thermoelectric semiconductor

Thermoelectric technology is an energy conversion technique capable of converting heat directly into electricity and *vice versa*[1], which has various applications including power generation[2-3], refrigeration[4-5], sensor[6] and so on. The functional devices of thermoelectrics are typically composed of a series of n- and p-type semiconductors connected alternately in an electrical series and thermal parallel configuration[7-8].

High-efficient thermoelectric devices require that both n- and p-type materials exhibit superior thermoelectric performance, which is measured by the dimensionless figure of merit (zT). zT is expressed as $zT=S^2\sigma T/\kappa$, where S is the Seebeck coefficient, σ is the electrical conductivity, T is the absolute temperature and κ is the total thermal conductivity including the contributions from electronic thermal conductivity (κ_E) and lattice thermal conductivity (κ_L)[9]. Obtaining high zT, however, is challenging because the electrical properties (S, σ, and κ_E) of charge carriers show a strong coupling effect. By modifying the electrons/holes transport properties for n-/p-type materials, band engineering[10-12] is demonstrated to be one of the successful strategies for decoupling the above electrical transport properties and enhancing zT.

In addition to assessing thermoelectric performance (zT), the long-term survival thermoelectric devices typically necessitate that both n- and p-type materials possess similar physical and chemical properties. In practice, the devices often use the same matrix material for governing the durability and fatigue life[13-14]. For instance, Bi_2Te_3-based alloys[4-5] are commonly employed as

Received date: 2024-04-02; **Revised date:** 2024-05-20; **Published online:** 2024-06-13
Foundation item: National Natural Science Foundation of China (T2125008, 92263108, 92163203, 52102292, 52003198); Shanghai Rising-Star Program (23QA1409300); Innovation Program of Shanghai Municipal Education Commission (2021-01-07-00-07-E00096)
Biography: MENG Yuting (1999–), female, Master candidate. E-mail: 2130605@tongji.edu.cn
孟雨婷(1999–), 女, 硕士研究生. E-mail: 2130605@tongji.edu.cn
Corresponding author: PEI Yanzhong, professor. E-mail: yanzhong@tongji.edu.cn; CHEN Zhiwei, associate professor. E-mail: 14czw@tongji.edu.cn
裴艳中, 教授. E-mail: yanzhong@tongji.edu.cn; 陈志炜, 副教授. E-mail: 14czw@tongji.edu.cn

matrix materials in commercial thermoelectric refrigerators, owing to their excellent thermoelectric performance at room temperature[15-17]. Si-Ge alloys[18-19] are applied to matrix materials in radioisotope thermoelectric generators (RTG) for the outstanding performance at high temperatures.

The discussion above suggests that the matrix materials with potential thermoelectric application need to possess both excellent electron and hole transport properties simultaneously. However, due to the opposite polarity of electrons and holes, the coexistence of electrons and holes (known as bipolar effect[20]) in such materials would compensate for their respective contributions to thermoelectric performance, leading to a rapid decay of total thermoelectric performance above the thermal excitation temperature. This is commonly observed in narrow band gap thermoelectric materials, where zT values of the materials increase with temperature increasing until bipolar effect occurs.

Due to the similar band degeneracies, effective masses and deformation potential coefficients (Table 1), the narrow-gap Bi_2Te_3-based[21-22] and $Bi_2(Te,Se)_3$-based[23-24] thermoelectric materials suffer bipolar effect above room temperature, accompanied with a detrimental effect on thermoelectric performance. Since the bipolar effect becomes severe when the concentration of electrons is equal to that of holes, an effective doping either donor or acceptor could efficiently suppress the bipolar effect, improving thermoelectric performance at such temperature.

Recently, the band engineering[25-27] and the microstructure engineering[17,23,28] strategies are employed to enhance the thermoelectric performance for Bi_2Te_3-based materials. The reported high peak zT values of 1.4 and 1.9 are achieved respectively in $Bi_{1.8}Sb_{0.2}Te_{2.7}Se_{0.3}$ + 15% (in mass) Te for n-type[29] and melt-spun $Bi_{0.5}Sb_{1.5}Te_3$ (with excess Te) for p-type[30], nearby the bipolar temperature. Therefore, the effects of modified band structure and modulated scattering charged carriers on the electron and hole transport properties are particularly important.

In this work, a two-band model, taking into account of the contribution of both majority and minority carriers, is utilized to quantify the crossover from single-band transport to two-band transport for Bi_2Te_3-based and $Bi_2(Te,Se)_3$-based thermoelectric materials with or without extrinsic doping. The band information of majority carriers can be identified in the single-band region, while the effect of minority is illustrated in the two-band region. Specifically, this work focuses on the influence of minority charged carriers on the Seebeck coefficient and Hall mobility in pristine Bi_2Te_3 single crystals along the in-plane direction. With further consideration of external scattering for charged carriers, the variations in the ratio of electron mobility to hole mobility in $Bi_2Te_{2.7}Se_{0.3}$ illustrate the manipulations on the bipolar effect.

1 Experimental

In this work, the Bi_2Te_3 and $Bi_2Te_{2.7}Se_{0.3}$ specimens were synthesized with the stoichiometric ratios by accurately weighing high-purity (99.99%) bismuth (Bi), tellurium (Te), and selenium (Se) elements. The elements were then mixed and loaded into the tapered end (with a 60° conical tip) of a glass tube with an inner diameter of 12 mm. The tube was evacuated and sealed, and the mixture was suspended in a furnace with vertically distributed temperature gradient. Based on the pseudo-binary phase diagram of Bi_2Te_3 and Bi_2Se_3, the furnace temperature was initially set at 1173 K (above the melting point) for 6 h. Subsequently, the temperature was cooled down to 893 K over a period of 2 h. Following this, a slow cooling process at a rate of 2 K/h was implemented until the temperature at each region of the ingot gradually descended below the melting point.

The crystal structure of Bi_2Te_3 belongs to the hexagonal crystal system, and its space group is $R\bar{3}m$ (Fig. 1). In the crystal structure of Bi_2Te_3, every five atomic layers form a charge-neutral layer. Along the c-axis, these five atomic layers are arranged in the order of Te(1)-Bi-Te(2)-Bi-Te(1), with the same atomic species within each layer. The numbers in parenthesis represent different Te positions, and Te atoms and Bi atoms form octahedral coordination. Upon alloying with 10% Bi_2Se_3, Se atoms replace some of Te positions, and the formation energy of Se vacancies is lower, rendering their electron donors unable to absorb two electrons. Intra-layer Bi-Te forms polar covalent bonds, while inter-layer Te(1)-Te(1) exhibits weak van der Waals bonding. Consequently, Bi_2Te_3 displays pronounced anisotropy. The in-plane electrical conductivity of n-type Bi_2Te_3 is six times higher than the out-of-plane direction; in contrast, it is only three times higher in the out-of-plane direction for p-type

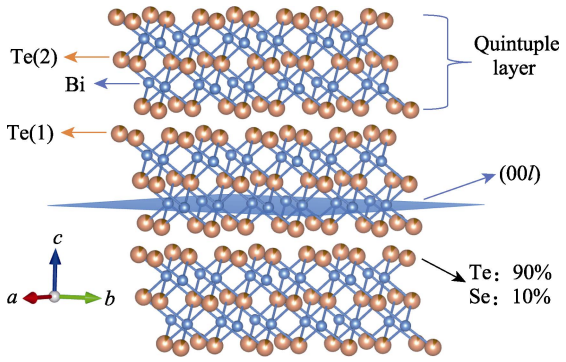

Fig. 1 Crystal structure of $Bi_2Te_{2.7}Se_{0.3}$

Bi_2Te_3[31-32]. Therefore, the crystal orientation significantly influences the thermoelectric performance. The Bi_2Te_3 and $Bi_2Te_{2.7}Se_{0.3}$ single crystals prepared in this study are primarily investigated in the in-plane direction. It can be observed from the powder X-ray diffraction (XRD) patterns that there is no obvious impurity phase in the material (Fig. 2(a)), while it can also be concluded from the single crystal XRD patterns that the materials are well oriented along the (00*l*) planes (Fig. 2(b)).

2　Single- and two-band transport property models

The electrons and holes in solids follow Fermi-Dirac distribution[33]. The fundamental parameters related to the charge carrier transport can be obtained by solving the Boltzmann transport equation in equilibrium[34-35]. The following equations used for the simulation calculations in this work can all be found in the relevant literatures[33-34, 36-37]. F_i in the following equations represents the Fermi integral of power exponent i.

$$F_i(\eta)=\int_0^{\infty}\frac{\varepsilon^i \mathrm{d}\varepsilon}{1+\exp(\varepsilon-\eta)} \tag{1}$$

$$n=4\pi\left(\frac{2m_{\mathrm{d}}^{*}k_{\mathrm{B}}T}{h^2}\right)^{\frac{3}{2}}F_{\frac{1}{2}} \tag{2}$$

$$S=\frac{k_{\mathrm{B}}}{e}\left(\frac{2F_1}{F_0}-\eta\right) \tag{3}$$

$$\sigma=\frac{8\pi e}{3}\left(\frac{2m_{\mathrm{d}}^{*}k_{\mathrm{B}}T}{h^2}\right)^{\frac{3}{2}}\mu_0 F_0 \tag{4}$$

where η is the reduced Fermi level ($\eta=E_{\mathrm{F}}/k_{\mathrm{B}}T$), E_{F} is the Fermi level, k_{B} is the Boltzmann constant (1.380649×10^{-23} J/K), n is the carrier concentration (cm^{-3}), m_{d}^{*} is the density of states effective mass (g), h is the Plank constant (6.6260693×10^{-34} J·s) and e is the elementary charge ($1.602176634\times10^{-19}$ C). The Seebeck coefficient (S) is a function of η, so the change of m_{d}^{*} can be judged by the Seebeck coefficient *versus* the carrier concentration[34]. It should be noted that the Hall carrier concentration (n_{H}) calculated by the Hall coefficient is not equal to the actual carrier concentration, and the two can be converted by the formula $n_{\mathrm{H}}=n/A$, where A is the Hall factor (Eq. 5)[34]. A similar Hall mobility (μ_{H}) can also be obtained from Eq. 6, where μ_0 is the mobility in the case of non-degeneracy limit (Eq. 7)[37]. Here, $\hbar$ is the reduced Plank constant ($\hbar=h/2\pi$), C_{l} is the longitudinal elastic constant, m_{I}^{*} is the inertial effective mass, m_{b}^{*} is the band effective mass, Ξ is the deformation potential coefficient (eV) characterizing the effectiveness of acoustic phonons to scatter charge carriers[33].

$$A=\frac{3}{2}F_{\frac{1}{2}}\frac{F_{-\frac{1}{2}}}{2F_0^2} \tag{5}$$

$$\mu_{\mathrm{H}}=\frac{\sigma}{n_{\mathrm{H}}e}=\mu_0\frac{F_{-\frac{1}{2}}}{2F_0} \tag{6}$$

$$\mu_0=\frac{\pi e\hbar^4 C_{\mathrm{l}}}{\sqrt{2}m_{\mathrm{I}}^{*\frac{3}{2}}m_{\mathrm{b}}^{*\frac{3}{2}}(\kappa_{\mathrm{B}}T)^{\frac{3}{2}}\Xi^2} \tag{7}$$

The thermal conductivity of the material is composed of the electronic thermal conductivity and the lattice thermal conductivity. The electronic thermal conductivity can be obtained by the Wiedemann-Franz law (Eq. 8). Similar with S, the Lorenz constant (L) is related to the position of the Fermi level which can be obtained by Eq. 9[34].

$$\kappa_{\mathrm{E}}=L\sigma T \tag{8}$$

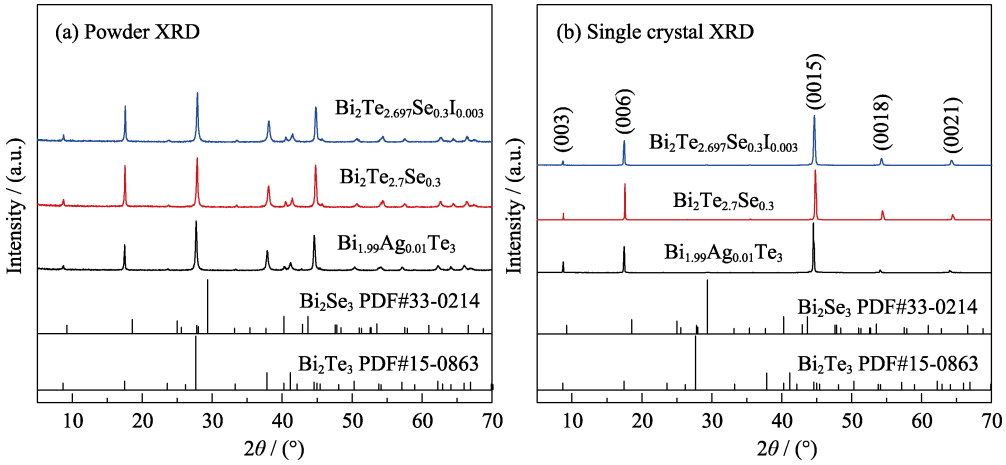

Fig. 2　XRD patterns of powder (a) and single crystal (b) specimens for $Bi_{1.99}Ag_{0.01}Te_3$, $Bi_2Te_{2.7}Se_{0.3}$ and $Bi_2Te_{2.697}Se_{0.3}I_{0.003}$

$$L=\frac{k_B^2}{e^2}\frac{3F_0F_2-4F_1^2}{F_0^2} \tag{9}$$

$$\kappa_L=\kappa-\kappa_E \tag{10}$$

The transport performance of narrow-band gap semiconductors can be predicted by appropriately weighted summation of the transport of each independent band[33]. The corresponding calculation relationship between conduction band and valence band is shown in Eq. 11, and the difference of Fermi levels between conduction band and valence band is the band gap (E_g) of the material. The total Seebeck coefficient (S_{total}) and conductivity (σ_{total}) can be obtained by the following equations:

$$\eta_n+\eta_p=-\frac{E_g}{k_BT} \tag{11}$$

$$S_{total}=\frac{S_n\sigma_n+S_p\sigma_p}{\sigma_n+\sigma_p} \tag{12}$$

$$\sigma_{total}=\sigma_n+\sigma_p \tag{13}$$

where the subscripts n and p denote the n- and p-type charged carriers. The total Hall coefficient ($R_{H,total}$) is weighted by the square of the electrical conductivity of each band from which the total Hall carrier concentration ($n_{H,total}$) and Hall mobility ($\mu_{H,total}$) can be defined[33]:

$$R_{H,total}=\frac{\mu_p^2n_p-\mu_n^2n_n}{(\mu_pn_p+\mu_nn_n)^2}\frac{1}{e} \tag{14}$$

$$n_{H,total}=\frac{1}{R_He} \tag{15}$$

$$\mu_{H,total}=\frac{\sigma_{total}}{n_{H,total}e} \tag{16}$$

The total thermal conductivity (κ_{total}) in the multi-band case has an additional bipolar thermal conductivity κ_{bi} besides the lattice and electronic thermal conductivity[33].

$$\kappa_{E,total}=L_n\sigma_nT+L_p\sigma_pT \tag{17}$$

$$\kappa_{bi}=\left[\sigma_nS_n^2+\sigma_pS_p^2-\frac{(\sigma_nS_n+\sigma_pS_p)^2}{\sigma_n+\sigma_p}\right]T \tag{18}$$

$$\kappa_{total}=\kappa_L+\kappa_{E,total}+\kappa_{bi} \tag{19}$$

3 Results and discussion

The electrical properties were characterized using an electrical performance measurement system[38-39] for Seebeck coefficient, electrical resistivity, and Hall coefficient. The Seebeck coefficient was determined by the slope of the thermopower with temperature gradient (with a temperature difference of approximately 5 K across the sample). The electrical resistivity and Hall coefficient were both measured using the van der Pauw method under a reversible magnetic field. The thermal conductivity was determined by measuring the thermal diffusivity (D) using the LFA457 and LFA467 instruments (NETASCH). The thermal conductivity (κ) was then calculated using the formula $\kappa=\rho C_pD$, where C_p is the specific heat capacity estimated using the Dulong-Petit law, and ρ is the material density.

Table 1 Parameters used in the two-band model for Bi_2Te_3 and $Bi_2Te_{2.7}Se_{0.3}$

Parameter	Bi_2Te_3	$Bi_2Te_{2.7}Se_{0.3}$
E_g/eV	0.14[24]	0.21[24]
$\mu_{0,VB,300\ K}$/($cm^2\cdot V^{-1}\cdot s^{-1}$)	369	265
$\mu_{0,CB,300\ K}$/($cm^2\cdot V^{-1}\cdot s^{-1}$)	487	214
Ξ_{VB}/eV	11.5	12.5
Ξ_{CB}/eV	10	13.8
$N_{v,VB}$	6	6
$N_{v,CB}$	6	6
$m_d^*{}_{,VB}/m_e$	1.06[24, 40-41]	1.4[42]
$m_d^*{}_{,CB}/m_e$	1.06[24, 41]	1.4[43-49]
$\kappa_{L,300\ K}$/($W\cdot m^{-1}\cdot K^{-1}$)	–	0.9

VB and CB denote the valence band and conduction band, respectively; N_v is the valley degeneracy

The thermoelectric transport properties of Bi_2Te_3 and $Bi_2Te_{2.7}Se_{0.3}$ can be estimated by two-band model. Witting *et al.*[24] have used the two-band model to simulate and calculate the Pisarenko lines of pure bismuth telluride material. In this work, the part of the two-band region is supplemented for comparison. The parameters used in the estimation are shown in Table 1.

The estimations are realized by shifting the Fermi level from the conduction band to the valence band. In this way, the Hall coefficient dependent Seebeck coefficient is just head to tail to form a closed curve that looks like the Arabic numeral "8" as shown in Fig. 3(a). Similarly, the Hall mobility *vs*. Hall coefficient form a closed curve as well (Fig. 3(b)). For the same R_H, the curve gives two possible S or μ_H, because of the compensation between majority and minority carriers. When the minority carriers are almost negligible, the Hall coefficient can be approximated as the inverse of the majority carrier concentration (Eq. 15), which is consistent with the approximation of the single parabolic band model. In this single-band region, the Seebeck coefficient and mobility increase with the increase of Hall coefficient, without obvious cancellation effect of minority carriers. When minority carriers gradually increase, the Hall coefficient decreases and gradually tends to 0 due to the reverse Hall effect by minority carriers. In such two-band region, the Seebeck coefficient and mobility

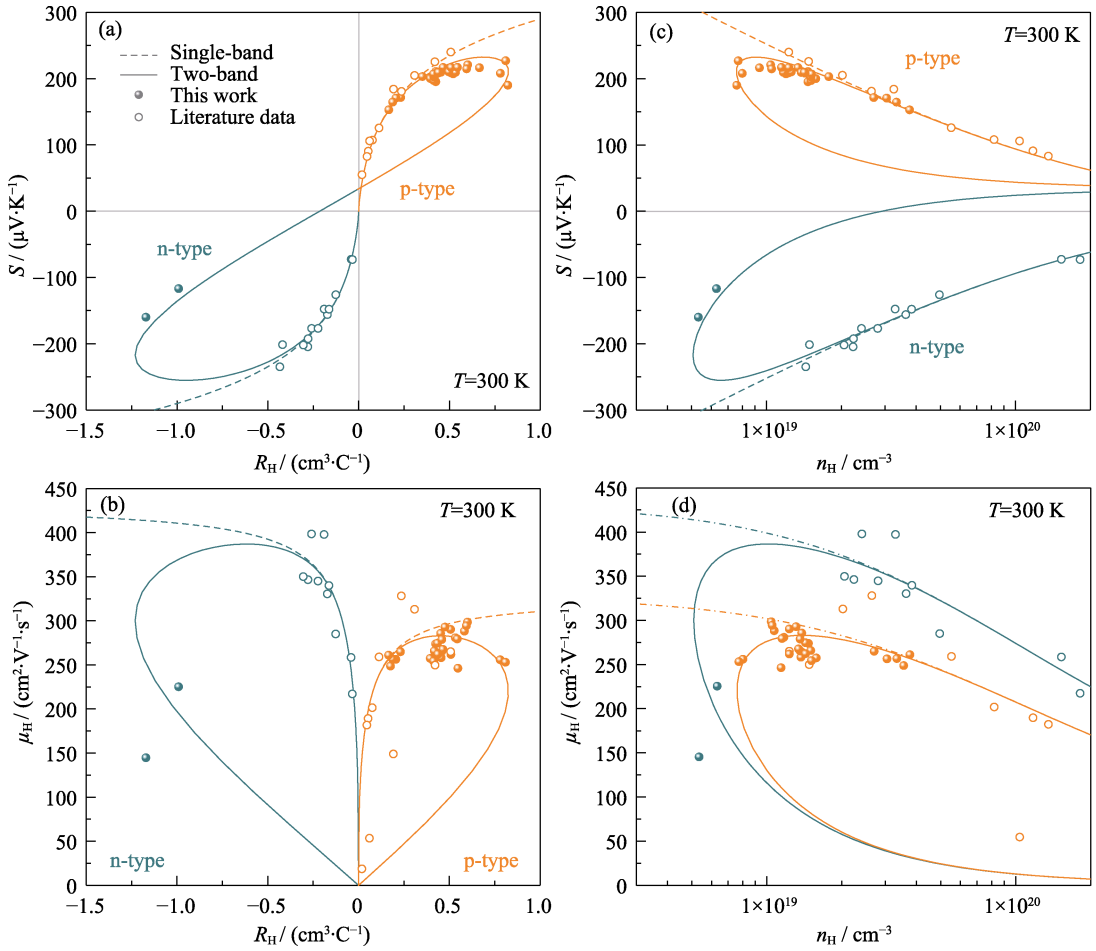

Fig. 3　Two-band model for n- and p-type Bi_2Te_3[24, 40-41] at room temperature

Seebeck coefficient (a, c) and Hall mobility (b, d) along the in-plane direction with respect to the Hall coefficient and Hall carrier concentration; Colorful figures are available on website

also decrease significantly due to the opposite sign between majority and minority carriers.

Fig. 3(c, d) give the conventional Pisarenko lines for better comparing the difference between the single-band region and the two-band region. When the material is heavily doped, the two-band curves (solid lines) of the Seebeck coefficient and Hall mobility as a function of Hall carrier concentration are consistent with the curves estimated by the single-band model (dashed lines). Accordingly, the density of states effective mass m_d* can be estimated from the change of Seebeck coefficient as a function of Hall carrier concentration. At 300 K, the density of states effective mass of both n- and p-type Bi_2Te_3 is $1.06m_e$ (Fig. 3(c)), which is consistent with similar analysis results in other studies[24, 40-41]. With the decrease of Hall carrier concentration, the curve gradually deviates from the estimation by single parabolic band. The deviation for Bi_2Te_3 occurs when the carrier concentration is 2×10^{19} cm^{-3}.

Similar estimations were carried out for $Bi_2Te_{2.7}Se_{0.3}$, as shown in Fig. 4. It is found that the density of states effective mass of both n- and p-type $Bi_2Te_{2.7}Se_{0.3}$ increase to $1.4m_e$ compared to Bi_2Te_3, which indicates the solid solution of Bi_2Se_3 can improve the band effective mass of Bi_2Te_3. At the same time, the deviation from the dash lines for $Bi_2Te_{2.7}Se_{0.3}$ occurs when the carrier concentration is 7×10^{18} cm^{-3}, which demonstrates that the solid solution of Bi_2Se_3 expands the band gap and inhibits the bipolar effect.

As shown in Fig. 4(c, d), the uncertainty in Hall mobility for $Bi_2Te_{2.7}Se_{0.3}$ is mainly attributed to the differences in mobility μ_0 caused by various factors, such as the change in scattering mechanisms and the possible anisotropy. The single crystal quality of n-type $Bi_2Te_{2.7}Se_{0.3}$ has the additional significant effect on the mobility. To reproduce and compare the experimental data collected from different literatures[42-49] and obtained in this work, the different mobility ratios ($\mu_{0,CB}/\mu_{0,VB}$) of conduction band and valence band are used in the model ($\mu_{0,VB}$ is approximated as a constant for avoiding too many variables). Changing the mobility ratio has little effect on the single-band region of the Seebeck and Hall coefficient. However, when the proportion of minority carriers gradually increases, the proportion of minority carriers

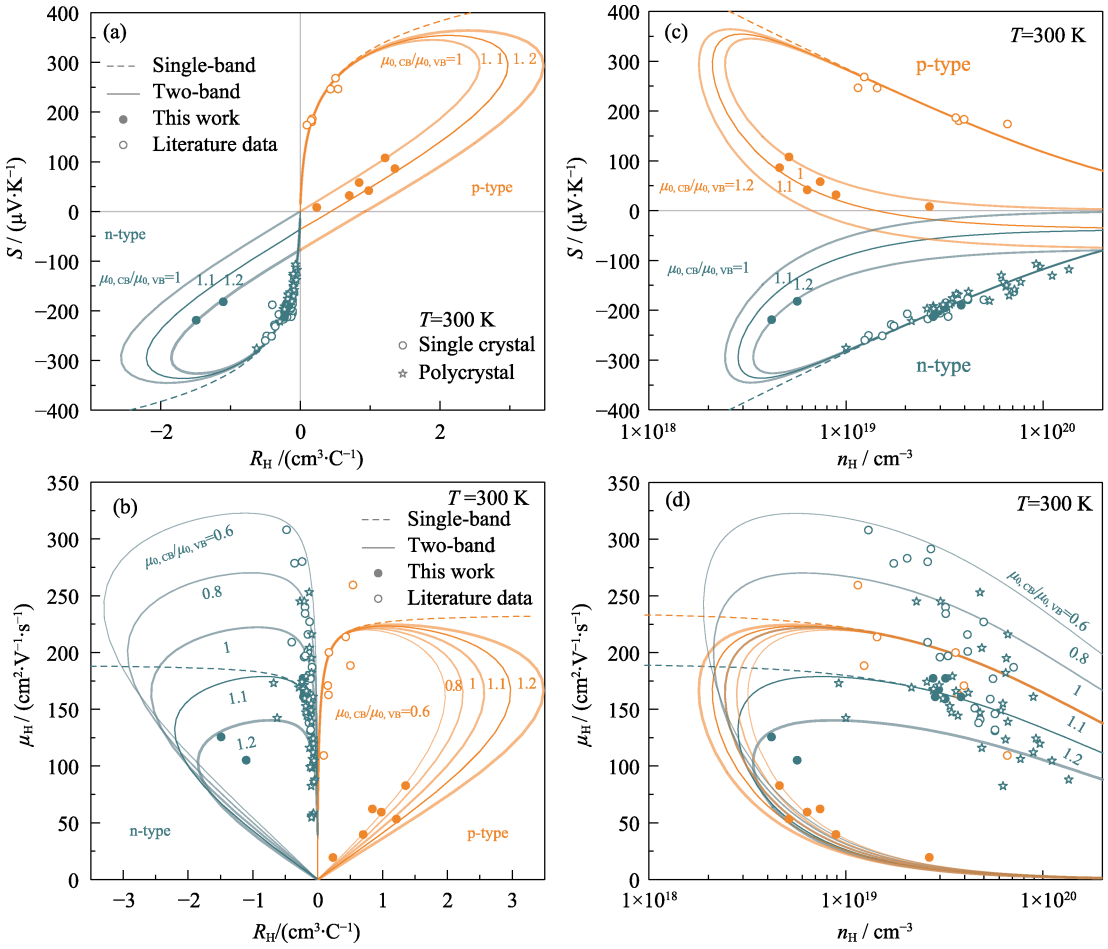

Fig. 4 Two-band model for n- and p-type $Bi_2Te_{2.7}Se_{0.3}$ at room temperature with different mobility ratios

Seebeck coefficient (a, c) and Hall mobility (b, d) along the in-plane direction[42-49] (circles) and random-orientation[50-53] (stars) with respect to the Hall coefficient and Hall carrier concentration, respectively; Varying thicknesses of the lines represents two-band curves simulated with different ratios of mobility for conduction and valence bands; Colorful figures are available on website

conductivity (depending on μ_0) increases accordingly, so that the compensate effect of minority carriers on Seebeck coefficient in two-band region is related to μ_0.

Fig. 5 shows the electrical conductivity (σ) dependence of thermoelectric performance estimated from the single- and two-band models. When the conductivity is lower than 200 $S \cdot cm^{-1}$, the Seebeck coefficient decreases sharply against the curve of the single-band model, which corresponds to the bipolar effect where carriers in both conduction and valence bands contribute significantly to transport (Fig. 5(a)). Due to the bipolar thermal conductivity, the total thermal conductivity (κ) in the low conductivity region increases dramatically (Fig. 5(b)), where the lattice thermal conductivity κ_L of $Bi_2Te_{2.7}Se_{0.3}$ single crystal along the in-plane orientation is estimated to be 0.9 $W \cdot m^{-1} \cdot K^{-1}$. It should be noted that the lower thermal conductivity for poly-crystalline samples (include parts of single-crystalline samples) could be understood by the existence of additional scattering sources for phonon transport, such as point defects and grain boundaries.

The maximum power factor (PF) along in-plane direction of $Bi_2Te_{2.7}Se_{0.3}$ is 40–50 $\mu W \cdot cm^{-1} \cdot K^{-2}$ at room temperature[48] (Fig. 5(c)). The room temperature zT values of n- and p-type $Bi_2Te_{2.7}Se_{0.3}$ in the literature are quite dispersed due to the wide-difference in μ_0 and κ (Fig. 5(d)), because microstructure engineering is often employed to reduce κ_L and improve zT. The room temperature zT of the I-doped n-type $Bi_2Te_{2.7}Se_{0.3}$ in this work is expected to achieve a peak of about 0.7 with σ ranging from 600 to 700 $S \cdot cm^{-1}$. For the better-quality single crystal, the maximum zT is almost above 0.9 at room temperature.

The thermoelectric transport properties of polycrystalline $Bi_2Te_{2.7}Se_{0.3}$ in different literature are also collected, as indicated by the star symbols in Fig. 4 and Fig. 5. The existence of a large number of grain boundaries increases the scattering strength of charge carriers. In single-band region, Seebeck coefficient is insensitive to the grain boundary scattering, which can significantly reduce the conductivity and mobility of polycrystalline $Bi_2Te_{2.7}Se_{0.3}$ (Fig. 4(d)). The lower textures of the polycrystal material would also reduce the conductivity of $Bi_2Te_{2.7}Se_{0.3}$ and

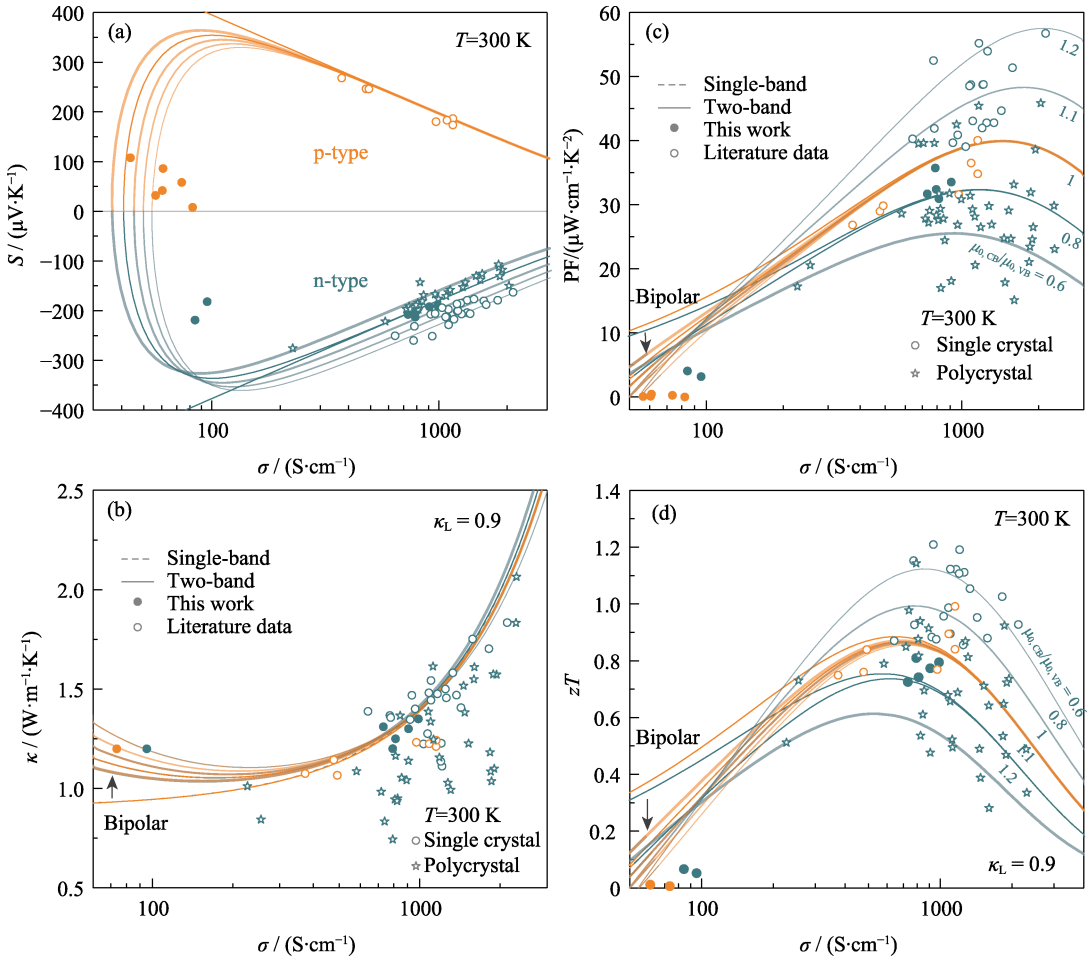

Fig. 5　Room-temperature Seebeck coefficient (a), total thermal conductivity (b), power factor (c), and zT (d) for n- and p-type $Bi_2Te_{2.7}Se_{0.3}$ (along the in-plane direction[42-49] and random-orientation[50-53]) as a function of electrical conductivity, along with the estimation by single-band (dashed lines) and two-band (solid lines) models
Colorful figures are available on website

thus reduce the power factor (Fig. 5(a, c)). At the same time, the existence of grain boundary also reduces the lattice thermal conductivity through additional phonon scattering (Fig. 5(b)). The literature works[54-56] often introduce point defects into polycrystalline materials to further reduce the lattice thermal conductivity for improving the thermoelectric performance of $Bi_2Te_{2.7}Se_{0.3}$. Therefore, it can be concluded from Fig. 5(d) that although zT values of $Bi_2Te_{2.7}Se_{0.3}$ materials are very dispersed due to the existence of strong anisotropy and different scattering mechanisms, zT values of single crystal and polycrystalline materials are nearly comparable.

4　Conclusions

This work employs the single- and two-band models to comprehensively illustrate the variations in thermoelectric transport properties of Bi_2Te_3 and $Bi_2Te_{2.7}Se_{0.3}$ in a wide range of Fermi level. Utilizing these models not only facilitate the effective analysis of fundamental material parameters such as m_d*, κ_L, and μ_0, but also provide a more intuitive representation of the changes in material properties under the influence of minority carriers, which is non-negligible in single-band model. This work presents accurate values for m_d* and κ_L, as well as the effect of μ_0 ratio on thermoelectric performance parameters. This offers a convenient tool for transport performance analyses when bipolar effect become severe in narrow gap thermoelectrics.

References:

[1] GOLDSMID H J. Applications of thermoelectricity. New York: Methuen, 1960**:** 1–7.
[2] SNYDER G J. Thermoelectric power generation: efficiency and compatibility//ROWE D M. Thermoelectrics handbook: macro to nano. Boca Raton: CRC/Taylor & Francis, 2006**:** 1–26.
[3] KRAEMER D, POUDEL B, FENG H P, *et al.* High-performance flat-panel solar thermoelectric generators with high thermal concentration. *Nature Materials*, 2011, **10(7):** 532.
[4] BELL L E. Cooling, heating, generating power, and recovering waste heat with thermoelectric systems. *Science*, 2008, **321(5895):** 1457.
[5] MAO J, CHEN G, REN Z. Thermoelectric cooling materials. *Nature Materials*, 2020, **20(4):** 454.

[6] PLATZEK D, KARPINSKI G, DRASAR C, *et al.* Seebeck scanning microprobe for thermoelectric FGM. *Materials Science Forum*, 2005, **492/493:** 587.

[7] BU Z, ZHANG X, HU Y, *et al.* A record thermoelectric efficiency in tellurium-free modules for low-grade waste heat recovery. *Nature Communications*, 2022, **13:** 237.

[8] MAO J, ZHU H, DING Z, *et al.* High thermoelectric cooling performance of n-type Mg_3Bi_2-based materials. *Science*, 2019, **365:** 495.

[9] CHEN Z, ZHANG X, PEI Y. Manipulation of phonon transport in thermoelectrics. *Advanced Materials*, 2018, **30(17):** e1705617.

[10] PEI Y, WANG H, SNYDER G J. Band engineering of thermoelectric materials. *Advanced Materials*, 2012, **24(46):** 6125.

[11] LI W, CHEN Z, LIN S, *et al.* Band and scattering tuning for high performance thermoelectric $Sn_{1-x}Mn_xTe$ alloys. *Journal of Materiomics*, 2015, **1(4):** 307.

[12] PEI Y, LALONDE A D, WANG H, *et al.* Low effective mass leading to high thermoelectric performance. *Energy & Environmental Science*, 2012, **5(7):** 7963.

[13] HE R, SCHIERNING G, NIELSCH K. Thermoelectric devices: a review of devices, architectures, and contact optimization. *Advanced Materials Technologies*, 2018, **3(4):** 1700256.

[14] SHARMA S, DWIVEDI V K, PANDIT S N. A review of thermoelectric devices for cooling applications. *International Journal of Green Energy*, 2014, **11(9):** 899.

[15] PEI J, CAI B W, ZHUANG H L, *et al.* Bi_2Te_3-based applied thermoelectric materials: research advances and new challenges. *National Science Review*, 2020, **7(12):** 1856.

[16] HONG M, CHEN Z G, ZIOU J. Fundamental and progress of Bi_2Te_3-based thermoelectric materials. *Chinese Physics B*, 2018, **27(4):** 048403.

[17] HU L P, ZHU T J, LIU X H, *et al.* Point defect engineering of high-performance bismuth-telluride-based thermoelectric materials. *Advanced Functional Materials*, 2014, **24(33):** 5211.

[18] AHMAD S, SINGH A, BOHRA A, *et al.* Boosting thermoelectric performance of p-type SiGe alloys through *in-situ* metallic YSi_2 nanoinclusions. *Nano Energy*, 2016, **27:** 282.

[19] ZHU G H, LEE H, LAN Y C, *et al.* Increased phonon scattering by nanograins and point defects in nanostructured silicon with a low concentration of germanium. *Physical Review Letters*, 2009, **102(19):** 196803.

[20] CHEN Z W, ZHANG X Y, REN J, *et al.* Leveraging bipolar effect to enhance transverse thermoelectricity in semimetal Mg_2Pb for cryogenic heat pumping. *Nature Communications*, 2021, **12:** 3837.

[21] TANG C, HUANG Z, PEI J, *et al.* Bi_2Te_3 single crystals with high room-temperature thermoelectric performance enhanced by manipulating point defects based on first-principles calculation. *RSC Advance*, 2019, **9(25):** 14422.

[22] SATTERTHWAITE C B, URE R W. Electrical and thermal properties of Bi_2Te_3. *Physical Review*, 1957, **108(5):** 1164.

[23] ZHANG Q, FANG T, LIU F, *et al.* Tuning optimum temperature range of Bi_2Te_3-based thermoelectric materials by defect engineering. *Chemistry – An Asian Journal*, 2020, **15(18):** 2775.

[24] WITTING I T, CHASAPIS T C, RICCI F, *et al.* The thermoelectric properties of bismuth telluride. *Advanced Electronic Materials*, 2019, **5(6):** 1800904.

[25] KIM H S, HEINZ N A, GIBBS Z M, *et al.* High thermoelectric performance in $(Bi_{0.25}Sb_{0.75})_2Te_3$ due to band convergence and improved by carrier concentration control. *Materials Today*, 2017, **20(8):** 452.

[26] MADAR N, GIVON T, MOGILYANSKY D, *et al.* High thermoelectric potential of Bi_2Te_3 alloyed GeTe-rich phases. *Journal of Applied Physics*, 2016, **120(3):** 035102.

[27] GREENAWAY D L, HARBEKE G. Band structure of bismuth telluride, bismuth selenide and their respective alloys. *Journal of Physics and Chemistry of Solids*, 1965, **26(10):** 1585.

[28] ZHU T, HU L, ZHAO X, *et al.* New insights into intrinsic point defects in V_2VI_3 thermoelectric materials. *Advanced Science*, 2016, **3(7):** 1600004.

[29] ZHU B, LIU X X, WANG Q, *et al.* Realizing record high performance in n-type Bi_2Te_3-based thermoelectric materials. *Energy & Environmental Science*, 2020, **13(7):** 2106.

[30] KIM S I, LEE K H, MUN H A, *et al.* Dense dislocation arrays embedded in grain boundaries for high-performance bulk thermoelectrics. *Science*, 2015, **348(6230):** 109.

[31] YAN X, POUDEL B, MA Y, *et al.* Experimental studies on anisotropic thermoelectric properties and structures of n-type $Bi_2Te_{2.7}Se_{0.3}$. *Nano Letters*, 2010, **10(9):** 3373.

[32] QIN C, JIN M, ZHANG R L, *et al.* Preparation and thermoelectric properties of ZnTe-doped $Bi_{0.5}Sb_{1.5}Te_3$ single crystal. *Mateials Letters*, 2021, **292:** 129619.

[33] GOLDSMID H J. Introduction to thermoelectricity. Heidelberg: Springer, 2009**:** 7–21.

[34] MAY A F, SNYDER G J. Introduction to modeling thermoelectric transport at high temperatures//ROWE D W. Materials, preparation, and characterization in thermoelectrics. New York: CRC Press, 2012**:** K1–K18.

[35] KIM M, KIM S I, KIM S W, *et al.* Weighted mobility ratio engineering for high-performance Bi-Te-based thermoelectric materials *via* suppression of minority carrier transport. *Advanced Materials*, 2021, **33(47):** 2005931.

[36] GOLDSMID H J. Thermoelectric refrigeration. New York: Plenum Press, 1964.

[37] KANG S D, SNYDER G J. Transport property analysis method for thermoelectric materials: material quality factor and the effective mass model. [2017-10-18]. https://arxiv.org/abs/1710.06896.

[38] DOS SANTOS C A M, DE CAMPOS A, DA LUZ M S, *et al.* Procedure for measuring electrical resistivity of anisotropic materials: a revision of the Montgomery method. *Journal of Applied Physics*, 2011, **110(8):** 083703.

[39] LEVY M, SARACHIK M P. Measurement of the Hall coefficient using van der Pauw method without magnetic field reversal. *Review of Scientific Instruments*, 1989, **60(7):** 1342.

[40] PLECHÁČEK T, NAVRÁTIL J, HORÁK J, *et al.* Defect structure of Pb-doped Bi_2Te_3 single crystals. *Philosophical Magazine*, 2004, **84(21):** 2217.

[41] NAVRATIL J, LOSTAK P, HORAK J. Transport coefficient of gallium-doped Bi_2Te_3 single-crystals. *Crystal Reserch and Technology*, 1991, **26(6):** 675.

[42] ZHANG Q, ZHAI R S, FANG T, *et al.* Low-cost p-type $Bi_2Te_{2.7}Se_{0.3}$ zone-melted thermoelectric materials for solid-state refrigeration. *Journal of Alloys and Compounds*, 2020, **831:** 154732.

[43] BIRKHOLZ U. Untersuchung der intermetallischen Verbindung Bi_2Te_3 sowie der festen Lösungen $Bi_{2-x}Sb_xTe_3$ und $Bi_2Te_{3-x}Se_x$ hinsichtlich ihrer Eignung als Material für Halbleiter-Thermoelemente. *Zeitschrift für Naturforschung A*, 1958, **13:** 780.

[44] HU L, WU H, ZHU T, *et al.* Tuning multiscale microstructures to enhance thermoelectric performance of n-type bismuth-telluride- based solid solutions. *Advanced Energy Materials*, 2015, **5(17):** 1500411.

[45] XIONG C L, SHI F F, WANG H X, *et al.* Achieving high thermoelectric performance of n-type $Bi_2Te_{2.79}Se_{0.21}$ sintered materials by hot-stacked deformation. *ACS Applied Materials & Interfaces*, 2021, **13(13):** 15429.

[46] WU G, TAN X J, YUAN M H, *et al.* High thermoelectric and mechanical performance in strong-textured n-type $Bi_2Te_{2.7}Se_{0.3}$ by temperature gradient method. *Chemical Engineering Journal*, 2023,

470: 144085.

[47] WANG S Y, TAN G J, XIE W J, *et al.* Enhanced thermoelectric properties of $Bi_2(Te_{1-x}Se_x)_3$-based compounds as n-type legs for low-temperature power generation. *Journal of Materials Chemistry*, 2012, **22(39):** 20943.

[48] HUANG W J, TAN X J, CAI J F, *et al.* Synergistic effects improve thermoelectric properties of zone-melted n-type $Bi_2Te_{2.7}Se_{0.3}$. *Materials Today Physics*, 2023, **32:** 101022.

[49] JARIWALA B, SHAH D, RAVINDRA N M. Transport property measurements in doped Bi_2Te_3 single crystals obtained *via* zone melting method. *Journal of Electronic Materials*, 2015, **44(6):** 1509.

[50] LI L, WEI P, YANG M J, *et al.* Strengthened interlayer interaction and improved room-temperature thermoelectric performance of Ag-doped n-type $Bi_2Te_{2.7}Se_{0.3}$. *Science China Materials*, 2023, **66(9):** 3651.

[51] KIM J H, CHO H, BACK S Y, *et al.* Lattice distortion and anisotropic thermoelectric properties in hot-deformed CuI-doped $Bi_2Te_{2.7}Se_{0.3}$. *Journal of Alloys and Compounds*, 2020, **815:** 152649.

[52] LEE G E, KIM I H, LIM Y S, *et al.* Preparation and thermoelectric properties of iodine-doped $Bi_2Te_{2.7}Se_{0.3}$ solid solutions. *Journal of the Korean Physical Society*, 2014, **65(5):** 696.

[53] LIU W S, ZHANG Q Y, LAN Y C, *et al.* Thermoelectric property studies on Cu-doped n-type $Cu_xBi_2Te_{2.7}Se_{0.3}$ nanocomposites. *Advanced Energy Materials*, 2011, **1(4):** 577.

[54] LI S J, CHEN T, YANG S H, *et al.* Attaining high figure of merit in the n-type $Bi_2Te_{2.7}Se_{0.3}$-Ag_2Te composite system *via* comprehensive regulation of its thermoelectric properties. *ACS Applied Materials & Interfaces*, 2023, **15(30):** 36457.

[55] JUNG Y J, KIM H S, WON J H, *et al.* Thermoelectric properties of Cu_2Te nanoparticle incorporated n-type $Bi_2Te_{2.7}Se_{0.3}$. *Materials*, 2022, **15(6):** 2284.

[56] ZOU P, XU G Y, WANG S, *et al.* Effect of high pressure sintering and annealing on microstructure and thermoelectric properties of nanocrystalline $Bi_2Te_{2.7}Se_{0.3}$ doped with Gd. *Progress in Natural Science: Materials International*, 2014, **24(3):** 210.

Bi_2Te_3 基热电材料的单带和双带传输特性转变

孟雨婷, 王雪梅, 章淑娴, 陈志炜, 裴艳中

(同济大学 材料科学与工程学院, 跨学科材料研究中心, 上海 201804)

摘 要: 基于 Peltier 效应, Bi_2Te_3 基合金被广泛应用于室温商用固态制冷。提高 Bi_2Te_3 室温热电性能的主流策略聚焦于能带和微结构工程。然而, 少数载流子部分补偿了窄带隙半导体 Bi_2Te_3 在室温下的宏观输运特性(即双极效应), 这使得人们深入理解能带结构、散射机制仍具挑战。本工作搜集了大量文献中 Bi_2Te_3 基热电材料的热电性能数据, 通过同时考虑多数载流子和少数载流子贡献的双带模型模拟了 Bi_2Te_3 基热电材料在双极效应区域附近和远离双极效应区域的热电输运特性。在模拟过程中, 将费米能级从导带过渡到价带以预测热电各项输运参数的变化情况, 并且量化了 Bi_2Te_3 基热电材料的各项基本参数, 如态密度有效质量、形变势系数等。该分析方法有助于找出提高 Bi_2Te_3 基合金热电性能的重要影响因素(如导带迁移率因子与价带迁移率因子的比值)。本工作为分析和预测材料在双极效应下的输运性能提供了一个方便的工具, 为窄带隙热电半导体的发展提供了有利的条件。

关 键 词: 热电材料; Bi_2Te_3 基合金; 双带模型; 窄带隙热电半导体

中图分类号: TB64　**文献标志码:** A　**文章编号:** 1000-324X(2024)11-1283-09